ADVANCED MATERIALS INTERFACES

Postfach 10 11 61
69451 Weinheim
Germany
Courier services:
Boschstraße 12
69469 Weinheim
Germany
Tel.: (+49) 6201 606 235
Fax: (+49) 6201 606 500
E-mail: advmatinterfaces@wiley.com

WILEY-VCH

Dear Author,

Please correct your galley proofs carefully and return them no more than four days after the page proofs have been received.

Please limit corrections to errors already in the text; cost incurred for any further changes or additions will be charged to the author, unless such changes have been agreed upon by the editor.

The editors reserve the right to publish your article without your corrections if the proofs do not arrive in time.

Note that the author is liable for damages arising from incorrect statements, including misprints.

Please note any queries that require your attention. These are indicated with a Q in the PDF and a question at the end of the document.

Reprints may be ordered by filling out the accompanying form.

Return the reprint order form by fax or by e-mail with the corrected proofs, to Wiley-VCH : advmatinterfaces@wiley.com

To avoid commonly occurring errors, **please ensure that the following important items are correct** in your proofs (please note that once your article is published online, no further corrections can be made):

- **Names** of all authors present and spelled correctly
- **Titles** of authors correct (Prof. or Dr. only: please note, Prof. Dr. is not used in the journals)
- **Addresses** and **postcodes** correct
- **E-mail address** of corresponding author correct (current email address)
- **Funding bodies** included and grant numbers accurate
- **Title** of article OK
- All **figures** included
- **Equations** correct (symbols and sub/superscripts)

Corrections should be made directly in the PDF file using the PDF annotation tools. If you have questions about this, please contact the editorial office. The corrected PDF and any accompanying files should be uploaded to the journal's Editorial Manager site.

Author Query Form

WILEY

Journal ADMI

Article admi201800957

Dear Author,

During the copyediting of your manuscript the following queries arose.

Please refer to the query reference callout numbers in the page proofs and respond to each by marking the necessary comments using the PDF annotation tools.

Please remember illegible or unclear comments and corrections may delay publication.

Many thanks for your assistance.

Query No.	Description	Remarks
Q1	Please provide TOC keyword.	
Q2	Please confirm that forenames/given names (blue) and surnames/family names (vermilion) have been identified correctly.	
Q3	Please provide the highest academic title (either Dr. or Prof.) for all authors, where applicable.	
Q4	Please provide postal code in all the affiliations.	
Q5	Please shorten Table of Contents text to a maximum of 60 words. All abbreviations should be defined.	
Q6	As per style, the experimental section has been moved to the end of the main text.	
Q7	Please check author name in ref. [28].	
Q8	Due to renumbering of sections, ref. [35] has been changed to ref. [34]; ref. [36] to ref. [35]; ref. [37] to ref. [36]; ref. [38] to ref. [37]; ref. [39] to ref. [38]; ref. [40] to ref. [39]; ref. [41] to ref. [40]; ref. [34] to ref. [41]. Please check.	
Q9	Please verify the inserted location in ref. [40] and provide editor names in ref. [40].	

Author: Please confirm that Funding Information has been identified correctly.

Please confirm that the funding sponsor list below was correctly extracted from your article: that it includes all funders and that the text has been matched to the correct FundRef Registry organization names. If a name was not found in the FundRef registry, it may not be the canonical name form, it may be a program name rather than an organization name, or it may be an organization not yet included in FundRef Registry. If you know of another name form or a parent organization name for a "not found" item on this list below, please share that information.

FundRef Name	FundRef Organization Name
Security Material Technologies Program	
National Research Council Canada	National Research Council Canada
Defense Research and Development Canada	

Q1 xxxx

P. Motamedi,* K. Bosnick, K. Cadien, J. D. Hogan 1800957

In Situ Synchrotron X-Ray Diffraction Analysis of Phase Transformation in Epitaxial Metastable hcp Nickel Thin Films, Prepared via Plasma-Enhanced Atomic Layer Deposition

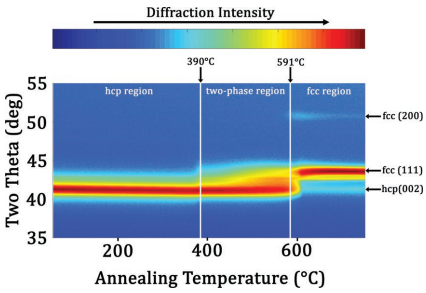

Epitaxial nickel thin films are prepared via atomic layer deposition. These films have a hexagonal crystal structure, as dictated by the sapphire substrate. The nickel hexagonal phase is metastable at lower temperatures. The effect of continuous heating of the films to various temperatures is investigated, and the nature of phenomena such as phase transformation and particle formation is discussed. Q5

ADVANCED MATERIALS INTERFACES
www.advmatinterfaces.de

In Situ Synchrotron X-Ray Diffraction Analysis of Phase Transformation in Epitaxial Metastable hcp Nickel Thin Films, Prepared via Plasma-Enhanced Atomic Layer Deposition

Q2 Pouyan Motamedi,* Ken Bosnick, Ken Cadien, and James D. Hogan

Ultrathin metal films have a wide variety of applications, especially in microelectronics. A key method to deposit these films is plasma-enhanced atomic layer deposition (PEALD), which is known for its ability to deposit thin films conformally and at relatively low temperatures. Building on the recent work, an improved recipe is reported on for the development of nickel PEALD technology, through which fully epitaxial nickel thin films are deposited. The effect of continuous heating on the phase structure and agglomeration in the metastable thin films is investigated in this paper. The variations of the phase structure are monitored via in situ synchrotron X-ray diffraction, as well as optical roughness analysis. The temperature windows for phase transformation and particle formation are determined. It is noted that, after the hcp-to-fcc transformation and particle coalescence processes are complete, the particles reshape to acquire the thermodynamically stable shapes dictated by the Wulff theorem. Additionally, a crystallographic orientation relationship between the fcc particles and the sapphire substrate is observed, i.e., Ni (111)||Sapphire(002).

1. Introduction

Metallic ultrathin films have a wide variety of applications in microelectronics,[1–3] energy storage,[4,5] catalysis,[6,7] and other areas. Specifically, multilayered structures of magnetic/non-magnetic ultrathin films are being increasingly researched for their potential applications in next generation information storage devices,[8,9] magnetic sensors,[10,11] magneto-optical devices,[12] thermoelectric devices,[13] and diluted magnetic semiconductors.[14] In all of these applications, the deposition of a relatively defect-free film and an atomic-level control over the thickness and the crystal structure are necessary requirements.[15,16]

Epitaxial growth of magnetic thin films enables the precise control of strain and crystal orientation, both of which have critical effects on the magnetization of thin films.[17,18] Another important benefit of epitaxial growth is limiting the grain boundary diffusion, which is shown to play a critical role in interlayer diffusion of the multilayer ultrathin films.[19,20] In order to fully realize the benefits of the ultrathin magnetic films, they need to be grown in an epitaxial fashion with a fine-tuned crystal structure and orientation. This subject is explored in the present paper.

Plasma-enhanced atomic layer deposition (PEALD) is a method for the deposition of Ni films that offers several advantages over more mainstream deposition methods, such as sputtering and chemical vapor deposition (CVD). These advantages include precise thickness control, relatively low growth temperature, and conformality, i.e., the ability to deposit a film with a uniform thickness over a non-flat substrate.[21–23] All of these benefits make this method suitable for growing ultrathin films, where thickness and structure are critical parameters.[24]

The authors have previously reported the plasma-enhanced ALD growth and characterization of nickel thin films with quasi-epitaxial crystal structure.[25] As reported, increasing the deposition temperature resulted in improving the crystallinity of the films. At deposition temperature of 360 °C, chemically pure nickel films were deposited. Crystal structure analysis showed the films had a polycrystalline textured structure with a strong out-of-plane orientation relationship with the sapphire substrate. However, full epitaxial growth was not achieved. This issue has been addressed in this paper.

Apart from the above-mentioned publication, there have been other recent reports on nickel deposition. Park et al.[26] recently reported on PEALD of nickel thin films using $[Ni(dpdab)_2]$ and NH_3 plasma, with the films reportedly having a fcc polycrystalline structure. In a separate study, Suturin et al.[27] demonstrated the deposition of epitaxial nickel islands on CaF_2 at 600 °C, using an electron beam source. The isolated islands had fcc crystal structure and crystallographic orientations dictated by that of the substrate. On a related subject, Tarachand et al.[28] investigated phase structure and magnetism in nickel nanoparticles grown by thermal decomposition, and reported that the

P. Motamedi, K. Bosnick
Nanotechnology Research Centre
National Research Council Canada
Q3 11421 Saskatchewan Dr., Edmonton, AB, Canada
E-mail: p.motamedi@ualberta.ca
P. Motamedi, J. D. Hogan
Department of Mechanical Engineering
University of Alberta
Q4 9211 116 St., Edmonton, AB, Canada
K. Cadien
Department of Chemical and Materials Engineering
University of Alberta
9211 116 St., Edmonton, AB, Canada
The ORCID identification number(s) for the author(s) of this article can be found under https://doi.org/10.1002/admi.201800957.

DOI: 10.1002/admi.201800957

particles are hcp/fcc mixture below 6 nm, but pure fcc above that size. A similar trend on the instability of hcp nickel had been reported earlier by Tian et al.[29] This was shown to have significant effects on the magnetism of the particles, which underscores the importance of crystal structure control in nickel thin films.

A review of these works and other earlier reports[30–33] related to nickel growth reveals a great interest in epitaxial growth of nickel on nonmagnetic and nonmetallic substrates, as well as in stabilizing hcp nickel for spintronics. Further to our previous work on nickel ALD,[25] we report the first successful deposition of epitaxial nickel using atomic layer deposition. This is, to the best of our knowledge, also the first time that direct epitaxy of hcp nickel films is reported using any deposition method.

Considering the fact that hcp nickel films are metastable, a complete understanding of the phase structure and its consequences on potential applications necessitates a comprehensive study of the behavior of the films at higher temperatures. Given the small thickness of the films, i.e., 20 nm, it is challenging to conduct a real-time analysis of isothermal annealing, since the films tend to undergo a certain amount of annealing during the heating stage. On the other hand, fast heating rates would expose the films to thermal shock. Therefore, an in situ study of the annealing process of the films is offered under the continuous-heating regime, which provides the most reliable results. X-ray diffraction and optical roughness analyses were conducted simultaneously to analyze the phase transformation, agglomeration, and particle shape transformation in the films. The in situ analysis combined with the postannealing characterization of the particles using microscopy and X-ray diffraction provides a general understanding of the behavior of the metastable nickel thin films at high temperatures.

2. Results and Discussion

2.1. Preannealing Characterization of the Epitaxial Film

Q6 The crystal structures of the as-deposited films are analyzed using both a regular Bruker X-ray diffraction (XRD) instrument (**Figure 1**) and synchrotron XRD in a θ–2θ geometry (**Figure 2**). A 2D XRD frame of the nickel films is shown in Figure 1a. In this frame, 2θ increases from right to left, while ψ, an out-of-plane rotation angle, increases upward along the denoted arc. The geometry of this setup has previously been explained in detail in refs. [32,33]. In a 2D XRD frame, any diffraction in the form of a concentrated spot indicates preferred orientation for that particular plane. A diffraction in the form of an arc, on the other hand, shows random orientation of the plane. A 2D frame of a polycrystalline sample without preferential orientation will consist of arcs with even intensity distribution for every allowed Bragg reflection. In the case of quasi-epitaxy, a subset of these arcs will show uneven distribution of intensity along ψ, and some allowed reflections may disappear.

Figure 1a features one heavily-concentrated reflection corresponding to sapphire (006) and nickel (002) planes. The shape of the (002) reflection, combined with the absence of nickel (100) and (101) reflections indicates that the nickel thin film has an epitaxial crystal structure with a strong crystallographic orientation relationship with the sapphire substrate, in such a way that the (002) nickel plane is parallel to the (006) plane of sapphire. Pole figures were used to further explore the orientation of the nickel crystal planes. Figure 1b shows the stereographic projection of hcp (002) pole figure of the as-deposited nickel film. This represents the overall distribution of (002) plane normals, with respect to the normal to the specimen surface. The concentrated intensity at the center clearly shows that the (002) plane normal vectors stand perpendicularly to the thin film, i.e., basal planes of the hcp nickel are parallel to the thin film surface. This is further confirmation of the epitaxial nature of the films.

Figure 2 shows the results of the XRD analysis performed at the synchrotron facility in the form of a 3D surface color map and its projection on 2θ-intensity and ω-intensity planes. The purpose of Figure 2 is to serve as a benchmark, against which the crystal structure of the annealed samples will be compared and analyzed. Figure 2a shows a 3D intensity graph, with a peak corresponding to nickel (002) and sapphire (006) planes. The projection of this graph on the 2θ-intensity plane shows a single peak, which is likely to be the sum of sapphire (006) and

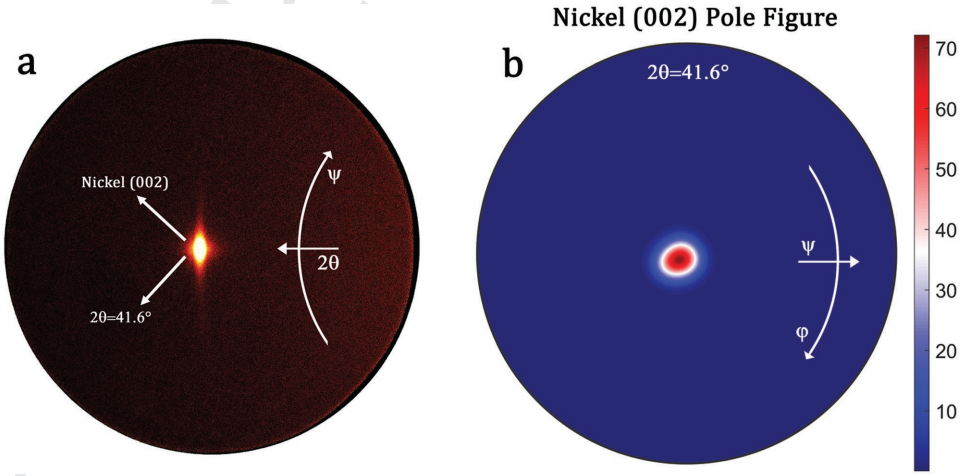

Figure 1. a) 2D XRD frame of the preannealing hcp nickel film, and b) pole figure obtained for (002) reflection of the same sample.

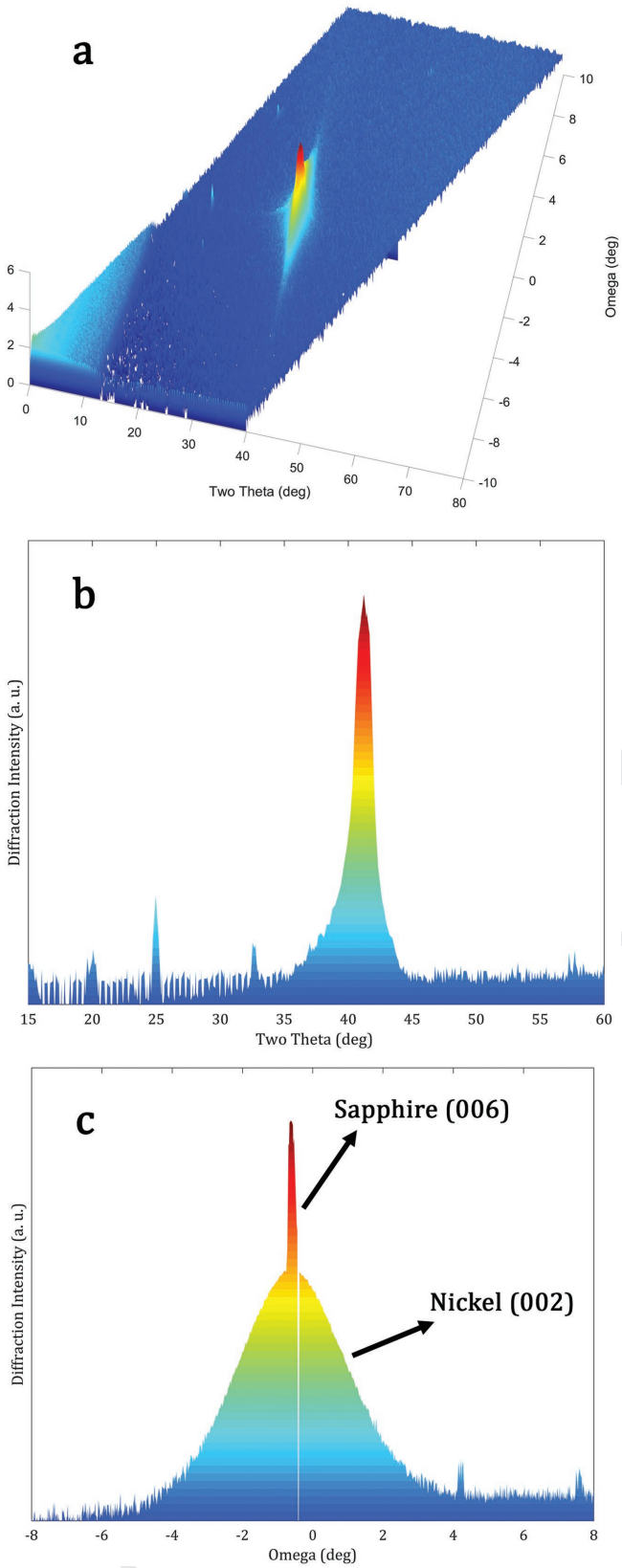

Figure 2. a) 3D graph of synchrotron θ–2θ XRD scan of the preannealing nickel film, b) the projection of the graph on 2θ-intensity plane, and c) the projection of the graph on ω-intensity plane.

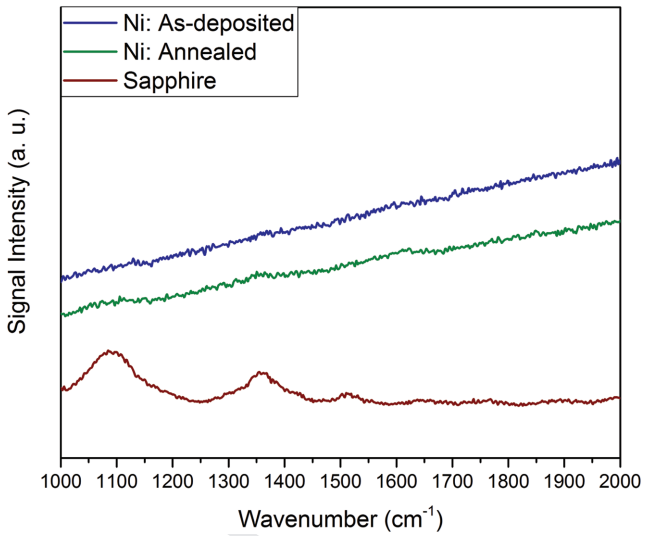

Figure 3. Raman spectra for the sapphire substrate, the as-deposited and the annealed nickel films.

nickel (002) peaks. In order to distinguish between the two, the projection on ω-intensity plane can be used (Figure 2c). Here it is clear that the peak is composed of a wide subpeak and a sharp one. Given the fact that the atomic order in the substrate is practically perfect, the sharp peak can be assigned to the substrate (sapphire (006)), and the spread-out peak to nickel (002). This notion will be experimentally verified and exploited in Section 2.2.1, where a slight deviation from the θ–2θ symmetrical setup allows for elimination of the sapphire peak, and isolation of nickel (002) peak.

One important factor to consider before studying the annealed films is to rule out the possibility of nickel carbide deposition. The Ni_3C phase, with the space group R-3cH, has a crystal structure very similar to that of metastable hexagonal nickel with the P63/mmc space group.[34,35] Nickel carbide is known to decompose to fcc nickel and graphite upon heating under inert gas.[36] The existence of graphite on our sample surfaces after annealing is checked for experimentally by Raman spectroscopy. **Figure 3** shows the Raman spectra for the sapphire substrate, as well as the preannealing and postannealing films. As observed, the absence of peaks normally associated with the graphite D- and G-bands confirms that graphite is either not present or is present in amounts lower than the detection limit of this test. Based upon this observation, the deposition of rhombohedral Ni_3C (instead of hcp Ni) can be ruled out. scanning electron microscopy (SEM)/EDX analysis (data not shown) further confirms the absence of gross graphite deposits on the surface after annealing.

2.2. Characterization of the Annealed Films

2.2.1. Phase Transformation Analysis

In order to observe and analyze the changes in the crystal structure of the nickel film during the annealing process, it is important to be able to isolate the (002) peak of the hcp nickel from

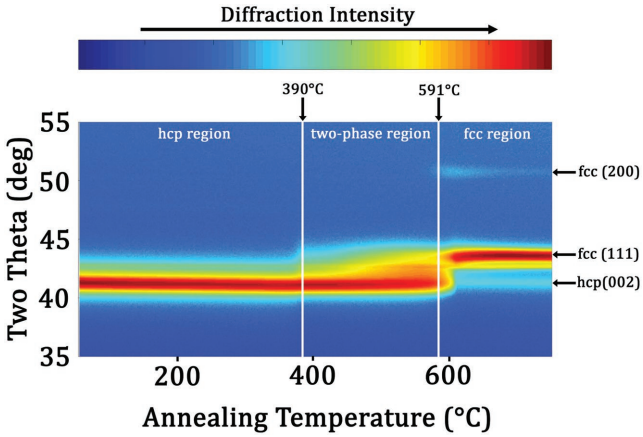

Figure 4. In situ variations of offset θ–2θ diffraction intensities as a function of the temperature; different zones are marked on the graph, which determine the phase structure of the film.

the overlapping (006) peak of the sapphire substrate. Since the sapphire peak showed a lower full width at half maximum, a slight deviation from the perfectly symmetrical θ–2θ geometry successfully isolates the signal from the nickel hcp peak. Positioning 2θ at 45.0° and θ at 21.2° allows for simultaneous monitoring of hcp (002) and potential fcc (111) and (200) peaks of nickel without significant interference from the (006) substrate peak.

The results of in situ X-ray diffraction of the hcp nickel film while heating from room temperature at the rate of 1 °C s^{-1} is shown in the form of a color map in **Figure 4**. Three regions can be distinguished on this map. No noticeable phase transformation occurs below 390 °C. In this temperature region the metastable hcp structure survives. The first signs of phase transformation are observed at ≈390 °C, where the hcp (002) peak begins to become diffuse and higher intensities are observed where the fcc (111) peak is expected to be observed. This indicates the beginning of disorganization in the hcp atomic structure of the epitaxial film. With increasing temperature, the hcp atomic order is further diminished, and the interatomic distances associated with the fcc (111) peak increases in intensity, which translates into a higher density of these planes. Eventually, when the temperature approaches 600 °C, the hcp (002) peak disappears completely, leaving only a diffuse fcc (111) peak, which later sharpens up. Another phenomenon which further validates the nature of this phase transformation is the formation of the fcc (200) peak at ≈52°.

In order to gain a better understanding of the crystal structure, four different samples were heated at the same heating rate of 1 °C s^{-1} to preset temperatures, and immediately quenched, upon reaching the target temperatures. The maximum temperature readings of the chamber pyrometer were 390, 563, 752, and 985 °C. The first three samples fall in each of the three temperature regions explained above, and the intention behind testing the fourth sample at 985 °C was to observe the further changes in the atomic structure, after the phase transformation was completed at ≈600 °C.

The results of the symmetrical θ–2θ coupled scans are shown in **Figure 5**. The insets show the projection of the graphs on 2θ-intensity plane. When compared with the as-deposited sample (Figure 2), the sample annealed to 390 °C shows a slight diffuseness of the peak toward the higher angles, which causes a slight asymmetry in the cross-section of the graph (inset of Figure 5a). The sample annealed to 563 °C (Figure 5b) shows signs of fcc (111) and (200) peaks, as clearly visible in the inset. However, the 3D graph in Figure 5b shows that the peaks are spread out along ω, which indicates the planes are not well-aligned. At 752 °C (Figure 5c), a well-shaped fcc (111) peak has formed, which indicates the completion of the hcp-to-fcc phase transformation. Further increase of the temperature in the fcc region leads to significant improvement in the alignment of the fcc lattice planes. This is manifested in much narrower distribution of the diffraction intensity along $\omega = 0$ line (Figure 5d).

2.2.2. Agglomeration and Particle Formation

Transmission electron microscopy was employed to obtain a better understanding of the overall structure and crystallography of the samples in the two-phase region. **Figure 6**a shows the overall structure of the film cross-section, on which different layers are marked. As seen, the morphology of the nickel film is that of a continuous film covered by sporadic islands. Figure 6b shows the intersection of one these of particles at a higher magnification. As seen, the continuity of the film has been disrupted and a particle has nucleated at this location. The observable diffraction contrast indicates a difference in crystal structure or orientation. This can be explained by the tendency of the thin films to minimize the total surface energy.[37] The surface energy in this system consists of two components: the nickel/sapphire interfacial energy and the free nickel surface energy. Both components can be minimized by transformation of the continuous film into discrete particles. This process happens through surface diffusion and migration of atoms towards dispersed nucleation sites.[38]

In order to better understand the transformation from a film to particles, the variations of the surface roughness were monitored via an in situ optical roughness measurement apparatus. The normalized results are shown in **Figure 7**. Three distinct regions can be identified on this image, based upon variations of the slope. In region I, the continuity of the original film is intact, and particle formation has not commenced. Particle coalescence and agglomeration occurs in region II. As seen, the rate of increase in roughness decreases with increasing temperature. This is expected, as the growing particles slowly run out of the continuous film, which acts as the source to feed nickel atoms to the particles. Finally, when particle growth is complete, particles start transforming toward their equilibrium shapes. This is discussed in detail in Section 2.2.3.

The postannealing surface profiles of the samples were analyzed using atomic force microscopy. The tapping mode images of the samples are shown in **Figure 8**, and the surface profile parameters of the samples obtained through image analysis are listed in **Table 1**. At 390 °C (Figure 8a), which is around the deposition temperature, the films are extremely smooth, and no signs of particles are observed. In the two-phase

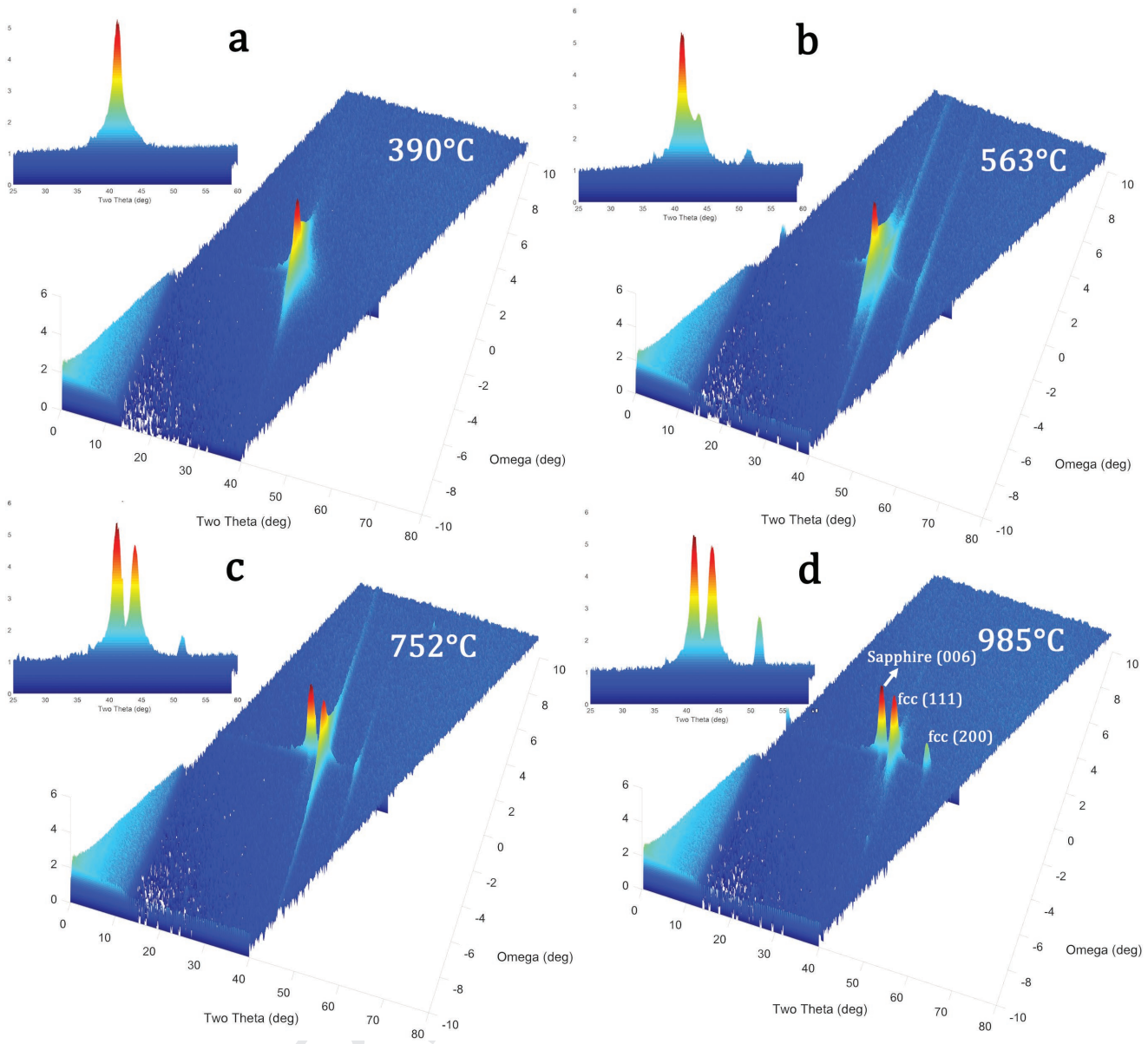

Figure 5. Post-annealing θ–2θ scans of the nickel films annealed to a) 390 °C, b) 563 °C, c) 752 °C, and d) 985 °C; the insets show the projections of the graphs on ω-intensity plane.

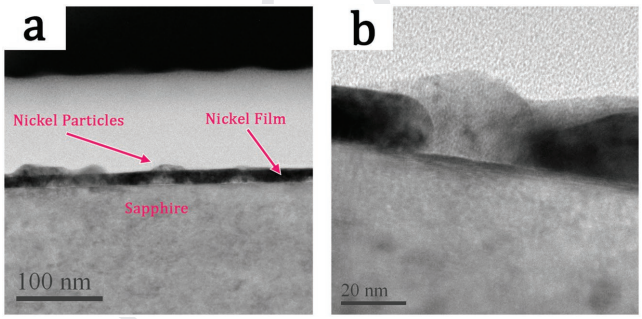

Figure 6. a) Transmission electron microscopy images of the cross-section of the nickel film annealed to 563 °C showing the overall structure, and b) the onset of particle formation.

region (Figure 8b), there is a relatively low density of particles. However, after increasing the temperature by 190 °C, and completion of the hcp-to-fcc phase transformation, the continuous film no longer exists (Figure 8c). The film has now completely transformed into particles with a mean diameter of ≈280 nm.

Up until this temperature, the effect of increasing the temperature was mainly on the nucleation of new particles, and the growth of the existing particles at the expense of the film. After the film-to-particle transformation is complete, further increase of the temperature leads to the second stage. At this stage the mean particle volume is conserved, but the particles reshape into a more symmetrical form (Figure 8d). At 985 °C, the particles show ≈21% decrease in the mean diameter and

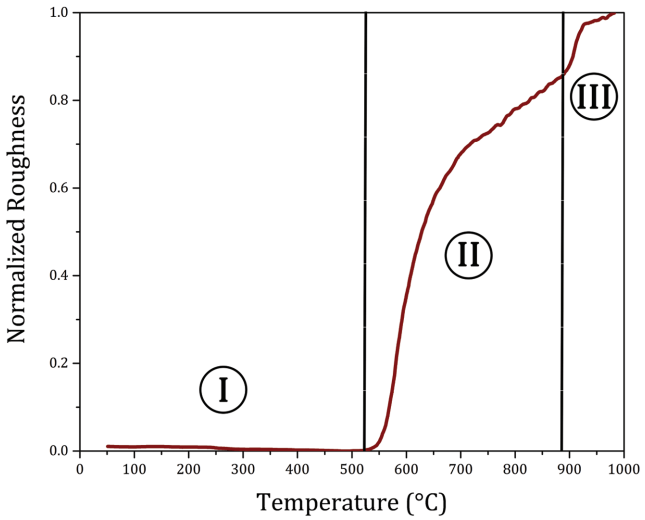

Figure 7. Variations of surface roughness during annealing; three distinct regions can be identified: continuous film (I), particle coalescence (II), and particle transformation (III).

≈60% increase in the mean height (Table 1). Observation of this second stage necessitates a closer examination of the sample annealed to 985 °C. It is also noteworthy that the coefficient of variation for particle height and diameter generally decrease with increasing temperature. This is indicative of intraparticle atomic migration.

2.2.3. Particle Shape Transformation and Alignment

Figure 9a shows, at a higher magnification, a 3D reconstruction of the surface profile of the sample annealed to 985 °C. As seen, the particles have a faceted outline and what looks like a common orientation. This can be further verified using scanning electron microscopy (Figures 9b,c). SEM images verify the fact that the particles have a polygonal footprint, close to that of a hexagon. Interestingly, the facets seem to be oriented parallel to common directions (Figure 9b).

In order to better understand the equilibrium shape of the nickel particles grown on sapphire, a simulation tool developed by Zucker et al.[39] was utilized. The software takes the values for the surface energies of various crystallographic planes and calculates the equilibrium shape of a free-standing as well as attached particle, based on the principles of the Wulff theorem. This theorem builds upon the concept that any solid has a natural tendency to minimize its Helmholtz free energy. Given the fact that for a given volume of a crystal with a specific crystal structure the bulk energy is constant, the equilibrium shape is determined in such a way as to minimize the total integrated surface energy of all crystal facets.[40]

The surface energy values used for the simulation are listed in **Table 2**. The ratio of the average nickel particle surface free energy to the nickel/sapphire interfacial energy does not affect the top-view outline of the particle or the ratio of the surface occupied by each crystallographic plane. Alternatively, it affects the contact angle of the particle on the surface. Since this

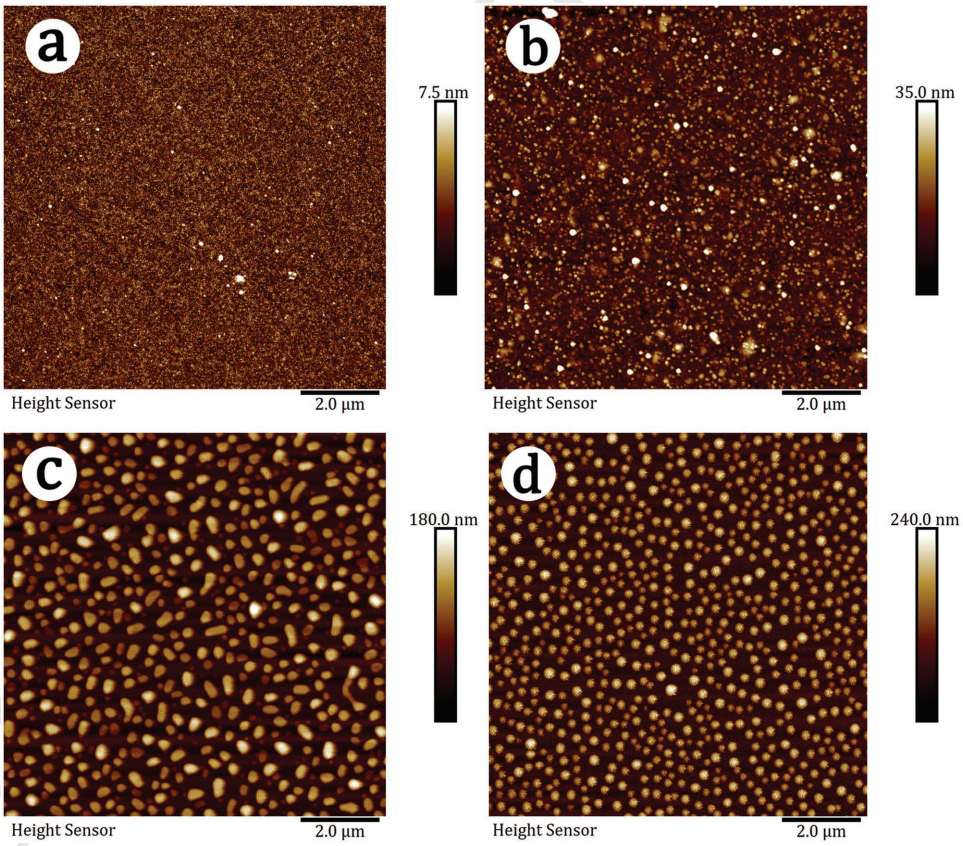

Figure 8. Tapping mode atomic force microscopy images of nickel thin films annealed to a) 390 °C, b) 563 °C, c) 752 °C, and d) 985 °C.

Table 1. Surface profile parameters of annealed nickel samples.

Temperature [°C]	Roughness[a)] [nm]	Particle diameter			Particle height		
		Mean [nm]	Sigma [nm]	Coefficient of variation	Mean [nm]	Sigma [nm]	Coefficient of variation
390	0.8	NA	NA	NA	NA	NA	NA
563	3.6	142.6	28.8	0.20	37.3	10.2	0.27
752	27.6	281.2	71.6	0.25	87.1	19.7	0.23
985	34.9	221.3	40.1	0.18	139.9	18.8	0.13

[a)]The arithmetic average of the roughness profile (R_a).

parameter is unknown, it is adjusted in such a way that the height-to-diameter ratio of the particles would match the experimentally observed value.

The top-view and side-view results of the simulation are shown in **Figure 10** It can be observed that when the (111) plane is attached to the substrate, the top-view outline of the particle resembles those observed experimentally. The top-view profile (Figure 10b) is similar to the top-view outline of the particles observed under SEM (Figure 10c). It is important to note that the shapes depicted in Figure 10 are only expected to be realized under the condition that enough atomic mobility exists, and a sufficient amount of time has passed. In the case of rapid heating processing, higher index planes are kinetically less likely to form, and therefore the final shape will mainly consist of low-index planes with sharper edges.

In order to further investigate the alignment of the crystallographic planes in the particles, the (111) pole figure for the sample annealed to 985 °C was obtained (Figure 10). As seen, there is a high concentration of intensity at the center, which shows the fcc (111) plane normals are standing perpendicularly to the substrate surface. In addition, there are three reflections at $\psi \approx 70°$. The three reflections are 120° apart in ϕ, which denotes a threefold symmetry. This describes the geometry of {111} plane family in fcc crystal structures. The inset of **Figure 11** shows the calculated shape of a particle for comparison, and demonstration of the symmetry. This pole figure confirms the SEM observations that showed the particle facets are aligned along the same common directions.

In summary, the shape of the nickel particles shows that {111} family of planes are situated at the nickel/sapphire interface, and the parallelism of the particle facets is a strong indicator that the particles and the substrate have a crystallographic orientation relationship. The obtained pole figures confirm this hypothesis. In other words, the atomic order in the particles is dictated by that of the top layer of the substrate. Considering the fact that the magnetic behavior of nickel nanoparticles is affected by their crystal orientation, this structure could be utilized in any application that requires fine-tuning of magnetism in metallic nanoparticles. This concept will be explored in our future studies.

3. Conclusion

The successful growth of epitaxial hcp nickel thin films on sapphire substrate via plasma-enhanced atomic layer deposition

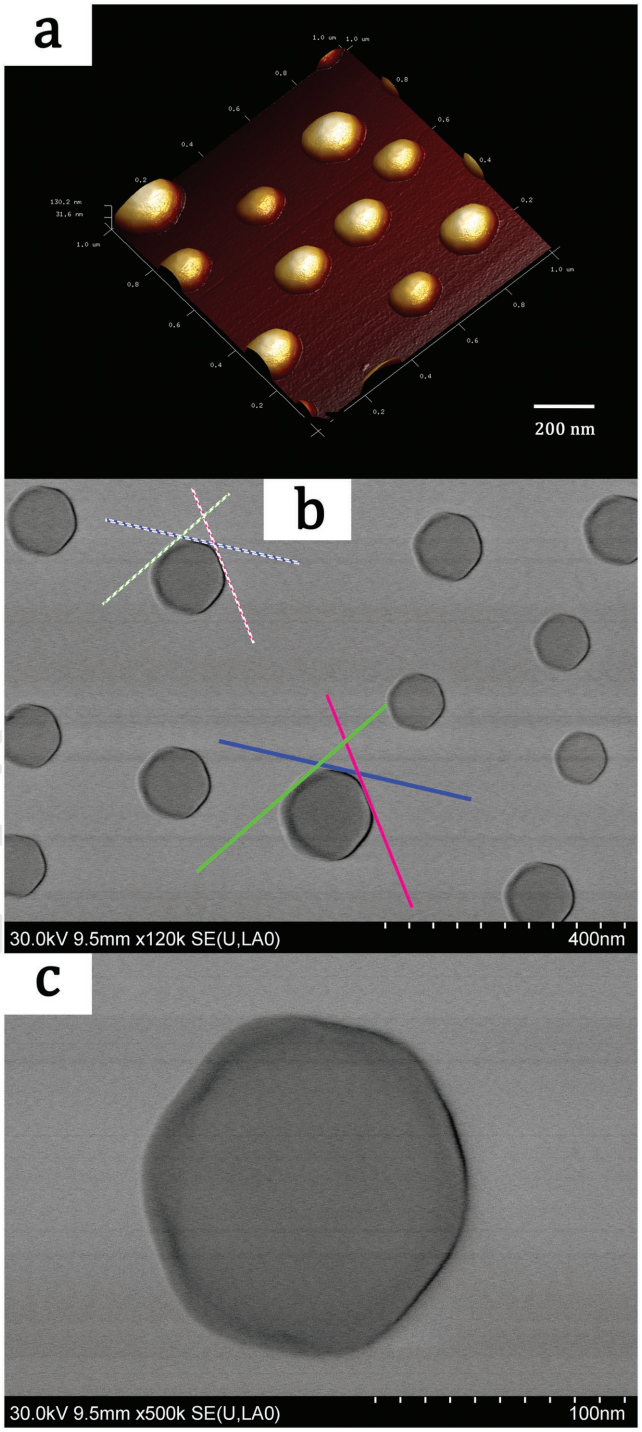

Figure 9. a) An AFM 3D reconstruction of nickel particles annealed to 985 °C and b,c) scanning electron micrographs of the particles from the same sample; the color lines highlight the parallelism of nickel particle facts.

was demonstrated. The metastable films were then annealed up to ≈1000 °C, while their crystal structure and roughness were continuously monitored. It was shown that two processes occur during annealing: hcp-to-fcc phase transformation, and film-to-particle transformation (agglomeration). The temperature

Table 2. Surface energy values used for the calculation of the equilibrium particle shape for fcc nickel.[42]

Crystallographic plane	Calculated surface energy [ergs per cm^2]
(100)	2434
(110)	2383
(111)	2035
(210)	2489
(211)	2335

windows for the two processes overlap at ≈550–600 °C. After the agglomeration was complete, the particles continued their transformation toward the thermodynamically stable shapes predicted by the Wulff theorem. The final particles featured identical top-view profile and smaller height and diameter variation. The particles show parallel facets and the obtained postannealing pole figure shows the particles have a common crystallographic orientation.

This work highlights the capabilities of PEALD in growing high-quality epitaxial metallic films with substrate-induced crystal structures and crystallographic orientations. Upon rapid annealing, these films transform into dispersed particles, which

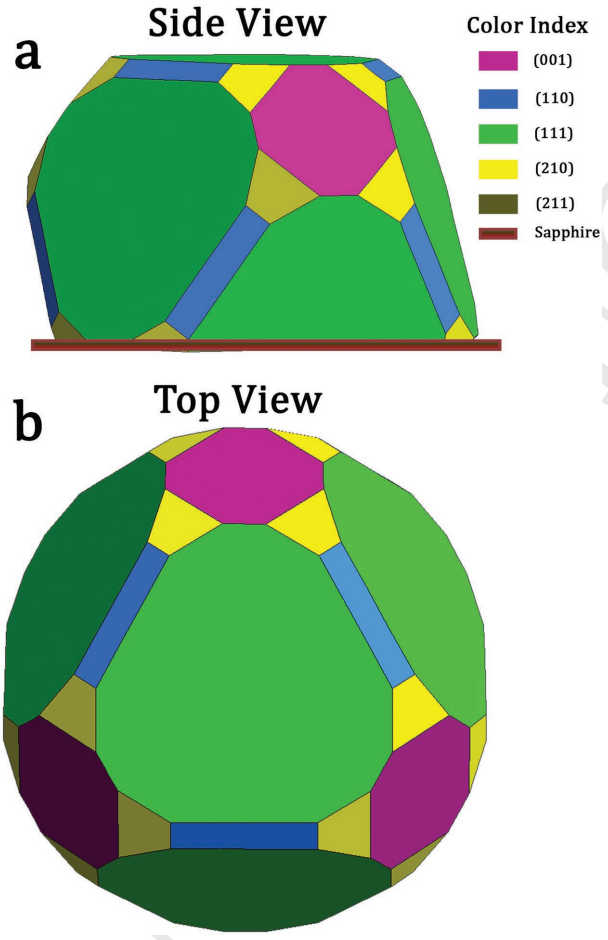

Figure 10. a) Side-view and b) top-view of the simulated equilibrium shape of a nickel fcc particle attached to a sapphire substrate via its (111) surface; various crystallographic planes are color-coded.

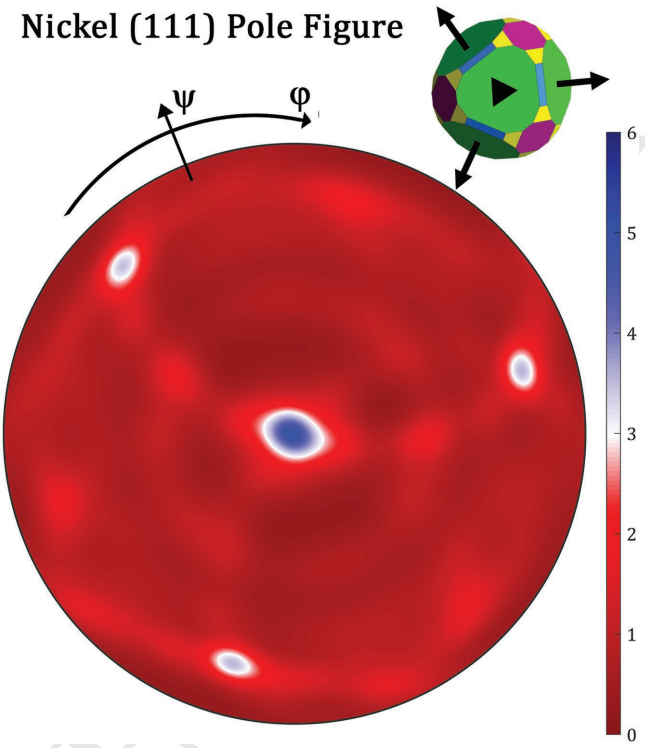

Figure 11. Pole figure of (111) fcc nickel, obtained from the sample of nickel particles annealed to 985 °C; the inset shows the calculated equilibrium shape of the fcc nickel particles with the threefold symmetry function.

acquire the same shape and orientation with respect to the crystallographic directions of the substrate. Both the preannealing and postannealing films have great potentials to be exploited in magnetic structures, where fine-tuned magnetism is important. The general findings of this article can be also used to develop similar technologies for other transition metal thin films and nanoparticles.

4. Experimental Section

Nickel thin films were deposited using a Kurt J. Lesker (ALD 150-LX) plasma-enhanced atomic layer deposition system. Bis(ethylcyclopentadienyl)-nickel ($Ni(EtCP)_2$), provided by Strem Chemical and $N_2/(5\%)H_2$ plasma were used as precursors. The precursor was heated to 100 °C, and the substrate temperature was kept at 385 °C. The pulse lengths for the organometallic and plasma were 10 and 30 s, respectively, and both purge times were set to 10 s. Depositions were carried out on *c*-plane sapphire. A growth rate of ≈0.5 Å per cycle was recorded for these parameters. The substrate was plasma cleaned for 120 s prior to the start of each deposition. Films with 20 nm thickness were chosen for characterization and annealing, in order to provide sufficient X-ray diffraction signal intensity.

The annealing was carried out under helium gas at the Ideas beamline of the Canadian Light Source synchrotron facility. The films were heated at the rate of 1 °C s^{-1} to the set temperatures and immediately cooled afterward. The films were monitored during the annealing via XRD in offset θ–2θ geometry and optical roughness analysis. The energy and the wavelength of the X-ray source were 8.02 keV and 1.546 Å, respectively. The detector was a HERMES-based photon-counting silicon microstrip, fabricated in-house at Brookhaven National Lab (BNL). A 655 nm pulsed

laser beam was used to assess the surface roughness. The angular distribution of the scattered monochromatic light was used to estimate the power spectral density of the surface topology.

2D XRD frames of the preannealing films were acquired using a Bruker D8-Discover machine, equipped with a Vantec 500 detector. The beam source was Cu kα, and the machine was set to 50 kV and 1000 µA. The same setup was used for acquiring pole figures. Pole figure data analysis was carried out using Bruker DIFFRAC.TEXTURE software, as well as MTEX toolbox for MATLAB.[41] Atomic force microscopy (AFM) was conducted using a Bruker Dimension Edge instrument, with tips from Bruker. All images were acquired in the tapping mode. Data analysis was carried out using the Nanoscope Analysis 1.5 software package. A Hitachi S-4800 field emission instrument was used for SEM. The secondary electron detectors were used for imaging. Transmission electron microscopy was accomplished using a Hitachi H9500 TEM and the data were analyzed with Gatan Digital Micrograph software.

Acknowledgements

The authors need to express their sincere gratitude to Dr. Joel Reid and Dr. David Muir at Canadian Light Source and Dr. Christian Lavoie at IBM T.J. Watson Research Center for their help with conducting in situ annealing analyses, as well as their insightful comments throughout the process. The authors also thank Dr. Douglas Vick and Dr. Kai Cui for their help with TEM sample preparation and operation. This work was funded via Security Material Technologies Program (National Research Council Canada) and by Defense Research and Development Canada.

Conflict of Interest

The authors declare no conflict of interest.

Keywords

ALD, annealing, epitaxy, nickel, XRD

Received: June 25, 2018
Revised: September 18, 2018
Published online:

[1] J. Schmitz, *Surf. Coat. Technol.* **2018**, *343*, 83.
[2] G. Scheunert, O. Heinonen, R. Hardeman, A. Lapicki, M. Gubbins, R. M. Bowman, *Appl. Phys. Rev.* **2016**, *3*, 011301.
[3] N. Choudhary, D. Kaur, *Sens. Actuators, A* **2016**, *242*, 162.
[4] N. Ali, A. Hussain, R. Ahmed, M. K. Wang, C. Zhao, B. U. Haq, Y. Q. Fu, *Renewable Sustainable Energy Rev.* **2016**, *59*, 726.
[5] K. Zhou, Z. Guo, S. Liu, J.-H. Lee, *Materials* **2015**, *8*, 4565.
[6] H. Jeong, J. W. Kim, J. Park, J. An, T. Lee, F. B. Prinz, J. H. Shim, *ACS Appl. Mater. Interfaces* **2016**, *8*, 30090.
[7] K. Bosnick, P. Motamedi, T. Patrie, K. Cadien, *MRS Adv.* **2017**, *2*, 1499.
[8] S. D. Pollard, J. A. Garlow, J. Yu, Z. Wang, Y. Zhu, H. Yang, *Nat. Commun.* **2017**, *8*, 14761.
[9] Y. Huang, W. Kang, X. Zhang, Y. Zhou, W. Zhao, *Nanotechnology* **2017**, *28*, 1.
[10] A. A. Chlenova, A. A. Moiseev, M. S. Derevyanko, A. V. Semirov, V. N. Lepalovsky, G. V. Kurlyandskaya, *Sensors* **2017**, *17*, 1900.
[11] C. Klever, M. Stüber, H. Leiste, E. Nold, K. Seemann, S. Ulrich, H. Brunken, A. Ludwig, C. Thede, E. Quandt, *Adv. Eng. Mater.* **2009**, *11*, 969.
[12] D. Guo, Y. An, W. Cui, Y. Zhi, X. Zhao, M. Lei, L. Li, P. Li, Z. Wu, W. Tang, *Sci. Rep.* **2016**, *6*, 25166.
[13] K. D. Lee, D. J. Kim, H. Yeon Lee, S. H. Kim, J. H. Lee, K. M. Lee, J. R. Jeong, K. S. Lee, H. S. Song, J. W. Sohn, S. C. Shin, B. G. Park, *Sci. Rep.* **2015**, *5*, 1.
[14] J. C. A. Huang, H. S. Hsu, Y. M. Hu, C. H. Lee, Y. H. Huang, M. Z. Lin, *Appl. Phys. Lett.* **2004**, *85*, 3815.
[15] U. Pohl, *Epitaxy of Semiconductors Introduction to Physical Principles*, Springer, Berlin, Germany **2013**.
[16] M. T. Johnson, P. Bloemen, F. J. A. den Broeder, J. J. de Vries, *Rep. Prog. Phys.* **1996**, *59*, 1409.
[17] A. Grutter, F. Wong, E. Arenholz, M. Liberati, A. Vailionis, Y. Suzuki, *Appl. Phys. Lett.* **2010**, *96*, 082509.
[18] X. Han, Q. Liu, J. Wang, S. Li, Y. Ren, R. Liu, F. Li, *J. Phys. D: Appl. Phys.* **2009**, *42*, 1.
[19] A. C. Lewis, D. Josell, T. P. Weihs, *Scr. Mater.* **2003**, *48*, 1079.
[20] X. L. Yan, Y. Liu, H. C. Swart, J. Y. Wang, J. J. Terblans, *Appl. Surf. Sci.* **2016**, *364*, 567.
[21] T. Kääriäinen, D. Cameron, M.-L. Kääriäinen, A. Sherman, *Atomic Layer Deposition: Principles, Characteristics, and Nanotechnology Applications*, Wiley, Salem, MA **2013**.
[22] R. W. Johnson, A. Hultqvist, S. F. Bent, *Mater. Today* **2014**, *17*, 236.
[23] J. Hämäläinen, M. Ritala, M. Leskelä, *Chem. Mater.* **2014**, *26*, 786.
[24] H. Kim, I. Oh, *Jpn. J. Appl. Phys.* **2014**, *53*, 03DA01.
[25] P. Motamedi, K. Bosnick, K. Cui, K. Cadien, J. D. Hogan, *ACS Appl. Mater. Interfaces* **2017**, *9*, 24722.
[26] J. Park, S. Kim, J. Hwang, W. S. Han, W. Koh, W. Lee, *J. Vac. Sci. Technol., A* **2018**, *36*, 01A119.
[27] S. M. Suturin, V. V. Fedorov, A. M. Korovin, N. S. Sokolov, A. V. Nashchekin, M. Tabuchi, *J. Appl. Crystallogr.* **2017**, *50*, 830.
[28] Tarachand, V. Sharma, J. Singh, C. Nayak, D. Bhattacharyya, N. Kaurav, S. N. Jha, G. S. Okram, *J. Phys. Chem. C* **2016**, *120*, 28354. Q7
[29] W. Tian, H. P. Sun, X. Q. Pan, J. H. Yu, M. Yeadon, C. B. Boothroyd, Y. P. Feng, R. A. Lukaszew, R. Clarke, *Appl. Phys. Lett.* **2005**, *86*, 131915.
[30] K. Heinz, S. Müller, L. Hammer, *J. Phys.: Condens. Matter* **1999**, *11*, 9437.
[31] M. Richard-Plouet, M. Guillot, S. Vilminot, C. Leuvrey, C. Estournès, M. Kurmoo, *Chem. Mater.* **2007**, *19*, 865.
[32] J. Gong, L. L. Wang, Y. Liu, J. H. Yang, Z. G. Zong, *J. Alloys Compd.* **2008**, *457*, 6.
[33] W. Kreuzpaintner, M. Störmer, D. Lott, D. Solina, A. Schreyer, *J. Appl. Phys.* **2008**, *104*, 114302.
[34] R. T. Chiang, R. K. Chiang, F. S. Shieu, *RSC Adv.* **2014**, *4*, 19488. Q8
[35] A. Furlan, J. Lu, L. Hultman, U. Jansson, M. Magnuson, *J. Phys.: Condens. Matter* **2014**, *26*, 415501.
[36] B. C. Bayer, D. A. Bosworth, F. B. Michaelis, R. Blume, G. Habler, R. Abart, R. S. Weatherup, P. R. Kidambi, J. J. Baumberg, A. Knop-Gericke, R. Schloegl, C. Baehtz, Z. H. Barber, J. C. Meyer, S. Hofmann, *J. Phys. Chem. C* **2016**, *120*, 22571.
[37] D. T. Danielson, D. K. Sparacin, J. Michel, L. C. Kimerling, *J. Appl. Phys.* **2006**, *100*, 083507.
[38] D. J. Srolovitz, M. G. Goldiner, *JOM* **1995**, *47*, 31.
[39] R V Zucker, D. Chatain, W. C. Carter, U. Dahmen, S. Hage, *J. Mater. Sci.* **2012**, *47*, 8290.
[40] T. L. Einstein, *Handbook of Crystal Growth*, Elsevier, Amsterdam **2015**, pp. 215–264. Q9
[41] F. Bachmann, R. Hielscher, H. Schaeben, *Solid State Phenom.* **2010**, *160*, 63.
[42] J. M. Zhang, F. Ma, K. W. Xu, *Appl. Surf. Sci.* **2004**, *229*, 34.

ADVANCED MATERIALS INTERFACES

Editorial office:
Wiley-VCH Verlag
Boschstraße 12, 69469 Weinheim
Germany

Tel.: (+49) 3047 031 331
Fax: (+49) 6201 606 500

Email: advmatinterfaces@wiley-vch.de

Reprint Order Form 2018

Short DOI: admi. _____

Please send me and bill me for

no. of **Reprints** via ☐ airmail (+ 25 Euro)
☐ surface mail

Please send me and bill me for a

☐ **high-resolution PDF file** (330 Euro).

My Email address:

_____

Please note: It is not permitted to present the PDF file on the internet or on company homepages.

Information regarding VAT

Please note that from German sales tax point of view, the charge for **Reprints, Issues or Posters** is considered as **"supply of goods"** and therefore, in general, such delivery is a subject to German sales tax. However, this regulation has no impact on customers located outside of the European Union. Deliveries to customers outside the Community are automatically tax-exempt. Deliveries within the Community to institutional customers outside of Germany are exempted from the German tax (VAT) only if the customer provides the supplier with his/her VAT number. The VAT number (value added tax identification number) is a tax registration number used in the countries of the European Union to identify corporate entities doing business there. It starts with a country code (e.g. FR for France, GB for Great Britain) and follows by numbers.

VAT no.: _____

(Institutes / companies in EU countries only)

Purchase Order No.: _____

Delivery address / Invoice address:
Name of recipient, University, Institute, Street name and Street number, Postal Code, Country

_____
_____
_____
_____
_____
_____
_____

Date and Signature: _____

Credit Card Payment (optional) -You will receive an invoice.

VISA, MasterCard, AMERICAN EXPRESS

Please use the Credit Card Token Generator located at the website below to create a token for secure payment. The token will be used instead of your credit card number.

Credit Card Token Generator:
https://www.wiley-vch.de/editorial_production/index.php

Please transfer your token number to the space below.

Credit Card Token Number

Price list for reprints (The prices include mailing and handling charges. All Wiley-VCH prices are exclusive of VAT)

No. of pages	Price (in Euro) for orders of 50 copies	100 copies	150 copies	200 copies	300 copies	500 copies
1-4	345	395	425	445	548	752
5-8	490	573	608	636	784	1077
9-12	640	739	786	824	1016	1396
13-16	780	900	958	1004	1237	1701
17-20	930	1070	1138	1196	1489	2022
for every additional 4 pages	147	169	175	188	231	315

Wiley-VCH Verlag GmbH & Co. KGaA; Location of the Company: Weinheim, Germany;
Trade Register: Mannheim, HRB 432833, Chairman of the Board: Mark Allin
General Partner: John Wiley & Sons GmbH, Location: Weinheim, Germany
Trade Register Mannheim, HRB 432296,
Managing Directors: Sabine Steinbach, Dr. Guido F. Herrmann

WILEY-VCH